13th International Symposium on Particle Image Velocimetry – ISPIV 2019
Munich, Germany, July 22-24, 2019

Optimization of Molecular Tagging Velocimetry for Shocked Particle Studies

John Charonko[1]*, J. Mike Mayer[1], Ankur Bordoloi[2], Kathy Prestridge[1]

[1]Los Alamos National Laboratory, Physics Division, Los Alamos, United States

[2]University of California, Berkeley, Civil and Environmental Engineering, Berkeley, United States

*john.charonko@lanl.gov

Abstract

Simulated and experimental MTV images have been analyzed with a technique commonly used to process grid images on surfaces, the Windowed Fourier Transform with Local Spectrum Analysis (WFT-LSA). A systematic synthetic image study of the Modulation Transfer Function (MTF) and error tendencies of the WFT-LSA was performed and compared with a PIV-style cross-correlation algorithm to see if advanced strategies such as iterative image deformation can improve analysis of gridded images with high noise levels. Testing of single-pass algorithms showed that in typical MTV images, the WFT-LSA yields significantly lower bias errors than cross correlation (CC) at displacements greater than 1 pixel but slightly higher random error at all displacements and image conditions. Analysis of the MTF of each algorithm shows that CC provided better resolution of spatial fluctuations than the WFT-LSA in many combinations of grid size and interrogation window. Tests of image deformation algorithms showed that the gap in performance between CC and WFT-LSA is maintained even as both methods improve. Additionally, simultaneous PIV and MTV experiments are planned for laminar and turbulent gas flow in a square channel. The PIV uses DEHS droplets for seeding, and is used as a baseline for testing the accuracy of various MTV algorithms. This will help isolate real-world effects introduced by the use of image intensifiers on the MTV camera that are hard to simulate like reduced signal-to-noise ratio, degraded spatial resolution, and phosphor decay time. Initial results have shown that these effects can be severe. After the completion of this study, the optimized setup will be installed in our horizontal shock tube for use in particle acceleration studies.

1. Introduction

Knowledge of the unsteady particle kinematics behind a shock wave is important for the understanding of many flows in extreme environments, such as supernovae and the distribution of blast debris in explosions. However, recent measurements of shock-accelerated particles indicate that drag coefficients are an order of magnitude larger than existing models would predict (Bordoloi et al. 2017). This discrepancy cannot be explained by current theory, and simulations in such regimes are extremely challenging. This leaves a need for experimental measurements of the flow around the accelerating particles to explain the unknown unsteady effects. Techniques like particle image velocimetry (PIV) and particle tracking (PTV) are limited by the response time of the tracer particles. Previous work has shown that many submicron-sized particles have temporal response on the order of 2-3 μs when crossing a shock, with properly dehydrated and filtered particles at best reaching 0.3 μs (Ragni et al. 2011). However, for the 4 μm particles used by Bordoloi et al, the measured time scales of their experiment were also 1-5 μs. This makes probing the background gas flow around a shock-accelerated particle using PIV or PTV impractical, even ignoring the difficulty in sufficiently seeding the flow. This problem can be overcome using molecular tagging velocimetry (MTV).

In MTV, the flow contains lag-free molecular tracers that are excited by a certain wavelength of light and will continue to emit photons after excitation. In gas-phase MTV, tracers can be generated with ambient air, such as excited-state oxygen (Miles and Lempert 1997) or they can be seeded into the flow. Molecules that

exhibit phosphorescence such as acetone and diacetyl are commonly used to seed a gas due to their high vapor pressures, relatively low toxicity, and need for only one photon source (Hiller et al. 1984). However, the phosphorescence of these molecules is quenched in the presence of oxygen, so phosphorescent tracers must be seeded into an oxygen-free medium. Previous experiments have utilized nitrogen (N_2) to eliminate this quenching effect (Stier and Koochesfahani 1999). We have chosen to use acetone-based MTV simultaneously with a particle tracking system to measure the flow field behind a shock, targeting simultaneous measurement of the particles' motion and the carrier phase gas velocity. The velocity is obtained through image analysis of the displacement of excited regions of the flow which often begin as a planar grid of laser lines and yield a two-component velocity vector (Koochesfahani and Nocera 2007).

However, in comparison to the extensive literature on the optimization of PIV processing and experiments, the analysis of MTV processing algorithms has to-date been more ad hoc in nature. In the past, spatial correlation techniques have been used in which a spatial correlation coefficient is calculated between the intensity field of a source window and the intensity field of a larger roam window (Gendrich and Koochesfahani 1996). More recently, use of a Hough transform algorithm based on line fitting has been proposed for analyzing MTV data (Sanchez-Gonzalez et al. 2015). In solid mechanics, the grid method is a well-established technique used to measure in-plane displacement and strain components on specimens undergoing small deformations. While various techniques exist to process grid images, the Windowed Fourier Transform (WFT) has become the most common processing method for this application (Grédiac et al. 2016). In this technique, the light intensity of the grid lines is expressed as a periodic signal with carrier phase modulations. Therefore, a slight displacement in the grid can be interpreted as a change in the signal's phase. Calculating the WFT of this signal returns a complex number map in the frequency domain. In the particular case that the WFT is applied with the frequency of the MTV grid, this procedure is called Local Spectrum Analysis (LSA). Even though other frequencies are not considered, very good results are still obtained, and the calculation time is much shorter (Surrel 1994). By computing only one frequency component in the FFT step, the velocity field can be computed at every pixel in the entire image with a single Fourier transform. This yields large increases in speed (>80x) compared to PIV-style algorithms. As far as we are aware, applying the WFT-LSA to MTV images has not been reported in literature.

In this work we will examine the advantages and disadvantages of the WFT-LSA approach for use in MTV applications as compared to a standard PIV-style cross-correlation algorithm. This will be done via systematic error analysis of representative synthetic images. In future work, we will apply the lessons learned from this study to shocked particle experiments currently under way at Los Alamos National Laboratory's Horizontal Shock Tube facility.

2. Methodology

2.1. The WFT-LSA algorithm

As described in Grédiac, Sur and Blaysat (2016), the WFT-LSA algorithm models the image field, $s(x,y)$, as function of some periodic fringe pattern frng() in x and y with a constant spatial frequency, f. These fringe functions are each modified by phase functions, ϕ_x and ϕ_y which dictate the displacement of the pattern in space.

$$s(x,y) = \frac{A}{2}\left(2 + \gamma \cdot \mathrm{frng}\left(2\pi fx + \phi_x(x,y)\right) + \gamma \cdot \mathrm{frng}\left(2\pi fx + \phi_x(x,y)\right)\right) \quad (1)$$

In the absence of image noise, A is the average image intensity; γ is the contrast of the fringe pattern relative to A; and the function frng() has a period of 2π, amplitude of 1, and an average value of 0.

The displacement of the pattern s between two times, $\mathbf{u}(\mathbf{x})$, can then be recovered from the difference of the vector phase maps, $\boldsymbol{\phi}^1$ and $\boldsymbol{\phi}^2$ such that $\boldsymbol{\phi} = (\phi_x, \phi_y)$, for two images with initial grid pitch $p = 1/f$:

$$\mathbf{u}(\mathbf{x}) = -\frac{p}{2\pi}\left(\boldsymbol{\phi}^2(\mathbf{x}+\mathbf{u}(\mathbf{x})) - \boldsymbol{\phi}^1(\mathbf{x})\right). \tag{2}$$

The problem of calculating the displacement field in the image pair s_1, s_2 then is reduced to the problem of finding the vector phase maps for each image. The phase of a periodic signal can be extracted from the image data using a 2D Fourier transform. Since we are interested in determining the local displacement at every point in the image data, not the mean displacement over the whole image, we can use a spatial weighting function, $g(x,y)$, to locally weight the Fourier transform, and slide this weighting function across the image, calculating the transform at every point. This weighting function should integrate to 1 to avoid modifying the amplitude of the image data. Then, the weighted Fourier transform, $\widehat{s_W}$, is defined as

$$\widehat{s_W}(x,y,\xi,\eta) = \int_{-\infty}^{+\infty}\int_{-\infty}^{+\infty} s(r,s)\, g(x-r, v-s)\, e^{-2i\pi(\xi r+\eta s)}\, dr\, ds. \tag{3}$$

The complex valued function $\widehat{s_W}$ then encodes the phase information for all frequencies (ξ, η) in the image at each point (x,y) as the angle of $\widehat{s_W}$ in the complex plane. However, since the fringe pattern frng() is dominated by its fundamental frequency f, most of the relevant information is encoded in the frequencies surrounding the points (f, 0) and (0, f) in the frequency domain. The WFT-LSA method simplifies the procedure for extracting the phase angles from $\widehat{s_W}$ by only considering and computing these two frequency components, and discarding the rest.

$$\widehat{s_{Wx}} = \widehat{s_W}(x,y,f,0) = \int_{-\infty}^{+\infty}\int_{-\infty}^{+\infty} s(r,s)\, g(x-r, v-s)\, e^{-2i\pi fr}\, dr\, ds \tag{4}$$

$$\widehat{s_{Wy}} = \widehat{s_W}(x,y,0,f) = \int_{-\infty}^{+\infty}\int_{-\infty}^{+\infty} s(r,s)\, g(x-r, v-s)\, e^{-2i\pi fs}\, dr\, ds \tag{5}$$

These are simply the convolution of either $s(x,y)e^{-2i\pi fx}$ or $s(x,y)e^{-2i\pi fy}$ with $g(x,y)$, which can be calculated very efficiently by computing these products and taking their FFT across the whole image domain, and then multiplying that by the FFT of $g(x,y)$. The phase functions are then computed as

$$\phi_x(x,y) = \text{angle}\left(\widehat{s_{Wx}}\right) \text{ and } \phi_y(x,y) = \text{angle}\left(\widehat{s_{Wy}}\right). \tag{6}$$

This yields the phase information at every pixel in the image. Contrast this process with a standard cross correlation used in PIV, which uses a similar spatial windowing step, but then usually requires a separate FFT (or directly calculated cross correlation) for every interrogation window. These windows are often overlapped by a significant degree, resulting in a much larger number of FFTs and a large amount of duplicated calculation.

Since these phase maps are often aliased, they need to be unwrapped to a consistent baseline. Here we used a MATLAB implementation (Kasim 2019) of the 2D phase-unwrapping algorithm as developed by Herráez et al. (2002).

Finally, using the phase maps recovered using eq. (6), the displacement is solved for using eq. (2). Since this expression requires knowledge of the displacement field, we can either solve for $\mathbf{u}(\mathbf{x})$ iteratively with

an initial guess, or directly in a single step using $\mathbf{u}(\mathbf{x}) = -\frac{p}{2\pi}\left(\boldsymbol{\phi}^2(\mathbf{x}) - \boldsymbol{\phi}^1(\mathbf{x})\right)$. According to Grédiac, Sur and Blaysat (2016), the iterative form is nearly converged after only a single iteration, but here we adopt the latter direct approach since we will be implementing the WFT-LSA displacement estimate as the kernel in a standard PIV-style iterative image deformation algorithm.

In the case where the initial grid lines are rotated relative to the camera axes and not necessarily orthogonal, we can compensate for this by adjusting two steps in the algorithm. First, in computing the local spectral components of the windowed FFT (eqs. (4) and (5)), we instead compute each in a rotated coordinate system, $\mathbf{x}'$ aligned with the matching grid line.

$$\begin{bmatrix} x' \\ y' \end{bmatrix} = \begin{bmatrix} \cos(\theta_1) & \sin(\theta_1) \\ \cos(\theta_2) & \sin(\theta_2) \end{bmatrix} \begin{bmatrix} x \\ y \end{bmatrix} \tag{7}$$

Here, θ_1 and θ_2 are the angles from the camera x-axis of each MTV grid line; in the case of $\theta_1 = 0$ and $\theta_2 = 90°$ these expressions simplify to $x' = x$ and $y' = y$. Once computed, x' and y' are substituted into the exponential terms in eqs. (4) and (5) and the Fourier transform of the new products $s(x,y)e^{-2i\pi fx'}$ or $s(x,y)e^{-2i\pi fy'}$ are computed as before for convolution with $g(x,y)$. Then, the phase maps are found as normal and a modified displacement field **u'** is solved for. To recover the displacements in the camera coordinate system we reverse this coordinate transform using the following relations:

$$\begin{bmatrix} u \\ v \end{bmatrix} = \begin{bmatrix} \cos(\theta_1) & \cos(\theta_2) \\ \sin(\theta_1) & \sin(\theta_2) \end{bmatrix} \begin{bmatrix} u' \\ v' \end{bmatrix}. \tag{8}$$

2.2. Error analysis with synthetic images

To analyze the performance of the WFT-LSA algorithm, the method was implemented within *prana*, an open source PIV code developed for MATLAB (https://github.com/aether-lab/prana). This allowed efficient access to a complete range of standard PIV-style analysis features such as iterative image deformation between displacement estimate passes, and outlier detection routines.

The method was tested on a series of synthetic images with varying grid geometry and image quality. The molecular tagging velocimetry grid images were simulated using a 2D grid of parallel lines with Gaussian profiles of thickness, T, defined as 4 times the standard deviation. Lines were separated by a grid spacing distance, GS, that was the same for both sets of perpendicular lines. Unless otherwise noted, the lines were oriented at 0 and 90° from the horizontal axis of the image. Grid spacing varied from $GS = 12$ to 36 pixels, and line thickness was between $T = 1.25$ to 12 pixels. The grid lines had a maximum intensity of 256 counts which was uniform across the image. There was a background intensity of 1% of the maximum, and normally distributed random noise was added to each pixel, ranging from 0 to 40% of the maximum grid intensity. After generating the first image, the second was created by interpolating the image based on the defined displacement field using 7th-order B-splines. Images were 512x512 pixels in size (see Figure 1).

The displacement field was either uniform, with x-displacement ranging from 0.1 to 18 pixels and a fixed 1 pixel displacement in y; or sinusoidal. The sinusoidal displacement function was given by:

$$u = \Delta x = 0; \quad v = \Delta y = V\sin(2\pi/\lambda \cdot x), \tag{9}$$

Here, V is the maximum displacement (half-amplitude) of the sinusoidal pattern. V was varied along with the wavelength, λ , (which ranged between λ=12-128 pixels) in order to maintain a constant maximum shear rate of $2\pi V/\lambda$ = 0.1 pixels/pixel-frame, or equivalently displacements between V=0.2 and 2.0 pixels.

Each image pair was processed either with the WFT-LSA algorithm described above, or with a standard FFT-based PIV cross-correlation algorithm using Gaussian filtering of the interrogation regions. To ensure a fair comparison, an identical windowing function was used for both algorithms. The effective resolution, W, of this window was varied between 24 and 120 pixels (Eckstein and Vlachos 2009). Displacement estimates were then used in an iterative image deformation algorithm, with up to 5 passes on same grid of sampling points with outlier removal and smoothing performed between iterations. Image interpolation was by 7th-order B-splines. Error analysis between the measured (u_m) and expected (u_e) displacements was performed on the raw unvalidated and unsmoothed displacements. These were calculated in terms of the random (σ), bias (β), and total (E) errors for each tested condition:

$$E^2 = \beta^2 + \sigma^2 = \sqrt{\frac{1}{N}\sum_{i=1}^{N}\left(u_{m,i} - u_e\right)^2}, \quad \beta = \overline{u_m} - u_e, \quad \sigma = \sqrt{\frac{1}{N}\sum_{i=1}^{N}\left(u_{m,i} - \overline{u_m}\right)^2}. \tag{10}$$

In each case, displacements near the borders of the images were excluded in order to avoid biasing the error statistics with measurements of incomplete interrogation regions.

In addition to error levels, the sinusoidal displacement field was analyzed in terms of the modulation transfer function (MTF) of the full processing algorithm (Astarita 2006).

$$MTF(\lambda) = 1 - \sqrt{\frac{\sum_{i=1}^{N}\left(v_i - v_e\right)^2}{\sum_{i=1}^{N}\left(V\sin\left(2\pi x/\lambda\right)\right)^2}} \tag{11}$$

The resulting MTF indicates how much the method attenuates fluctuations at a given wavelength under the assumption that the processing only decreases the amplitude of the measured signal, and does not corrupt it with random error, shifts in phase, or other artifacts.

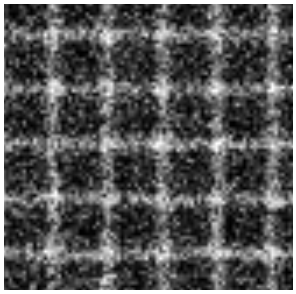

(a) uniform: GS = 24.2, T = 9, noise = 40%

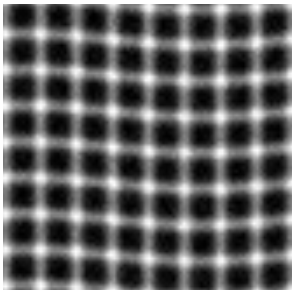

(b) sinusoidal: λ = 160, GS = 16, T=9, noise = 5%

Figure 1: Detail of 128x128 pixel sections of example synthetic images

3. Results

3.1. Error comparisons for uniform flow

Figure 2 shows the bias and random errors versus uniform displacement for the standard cross correlation (CC) and the WFT-LSA algorithms for range of spatial filter sizes and a fixed grid size of 24 pixels at a noise level of 5% . The WFT-LSA showed performance that was largely insensitive to displacement with bias errors averaging between 0.001 and 0.01 pixels, and random errors between 0.01 and 0.03 pixels except at the smallest window size which was the same size as the grid spacing, and had errors up to 0.2 pixels.

The bias error showed little effect of window size, while the random error was slightly smaller for larger windows. Standard cross correlation showed similar bias error levels as WFT-LSA for displacements around 1 pixel or less, but increased with larger displacement to 0.1 pixels or more with a much more pronounced window size effect. Random errors were nearly constant with a smaller effect from spatial window size than the bias error, and almost identical error magnitudes as WFT-LSA. Together, the total error for WFT-LSA was around 0.01-0.03 pixels regardless of displacement for window sizes greater than 24 pixels, while errors for the CC method were consistently higher and increased with displacement. Both methods showed a sudden increase in error as the displacement increase above half the imposed grid spacing, due to ambiguity in the aliasing of the periodic pattern.

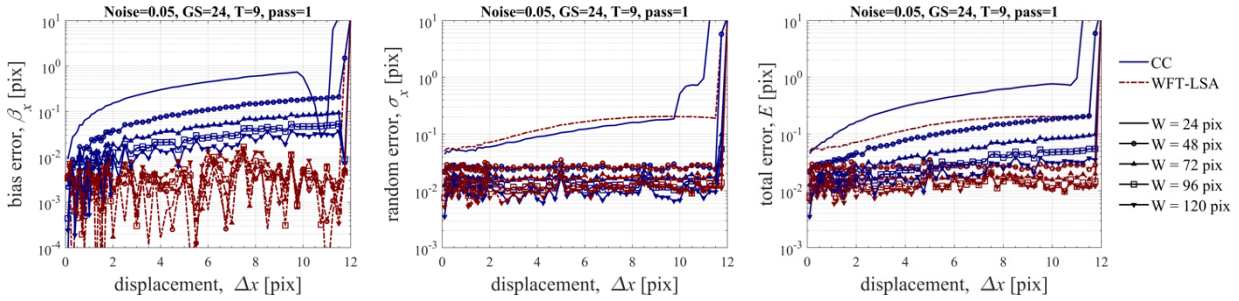

Figure 2: Error versus uniform displacement magnitude with *GS*=24 pix and varying window sizes. The absolute values of the bias errors are plotted; for the CC method they were everywhere negative.

To explore more fully the effects of the geometric parameters such as the grid spacing, thickness, angle, and the processing parameter of the spatial filter size, the remaining results will focus on uniform flow with u = 5.5 and v = 1.0 pixels, a grid spacing of either 24.2 or 24.4 pixels, and a line thickness of 9 pixels with 5% image noise. From this base condition, we will vary a single parameter and evaluate a range of spatial window sizes. Since the breakdown between bias error (larger for CC than for WFT-LSA) and random error (similar for both algorithms) were consistent across each tested parameter and showed similar trends, for conciseness we will only show total error.

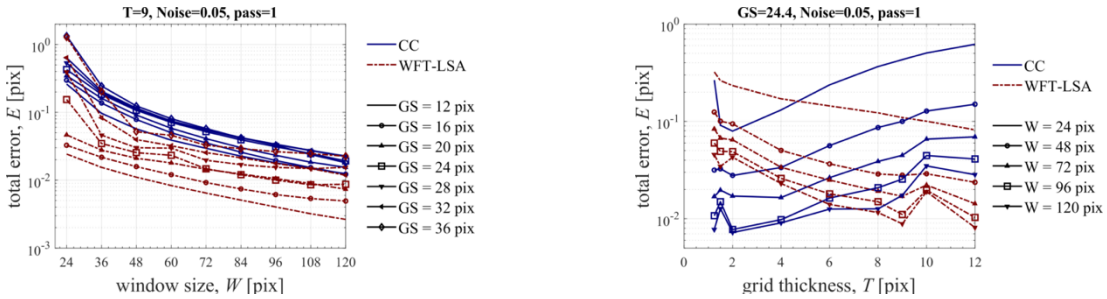

Figure 3: Total error versus window size (a) and grid thickness for images with uniform displacement.

As shown in Figure 3(a), error decreased with increasing window size for both algorithms. As before, errors were lower for WFT-LSA than for CC. The WFT-LSA algorithm showed a larger increase in error for more widely spaced grid lines than did the CC processing, and failed more quickly as the window size became smaller than the grid spacing. This is likely because the cross-correlation algorithm could take advantage of information about the displacement of the lines even when less than a full period was imaged, while the WFT-LSA was less able to compensate. Tests of variation in grid thickness revealed that like with traditional PIV images, cross-correlation of MTV grids shows a minimum error for grid thicknesses between about 2-3 pixels across. In contrast, the WFT-LSA method showed decreasing error all the way 12 pixels in width, which was the maximum tested. Although not investigated, it is hypothesized that this is because the wider grids put more energy into the FFT modes corresponding to the fundamental period of grid images than do the narrow lines, which contain much more energy in high frequency modes. The WFT-LSA

algorithm only samples this single mode, while the standard cross-correlation method incorporates signal from the entire frequency domain.

One of the defining features of many MTV experiments in air is a low signal level introduced by rapid decay of the phosphorescence signal. This is partly counteracted by the use of image intensifiers, but typically these also introduce additional noise into the images, resulting in an overall decrease in the signal-to-noise ratio. For uniform flows, the WFT-LSA maintains its performance lead over standard cross-correlation even up to 40% image noise (SNR=2.5) (Figure 4(a)). At this noise level, the PIV-style cross correlation yielded errors between 0.4-1.0 pixels, while the WFT-LSA kept the total error to 0.07-0.5 pixels. For a window size of 48 pixels, WFT-LSA was able to measure the displacement to within 0.1 pixels, while the total error was 0.5 pixels for CC.

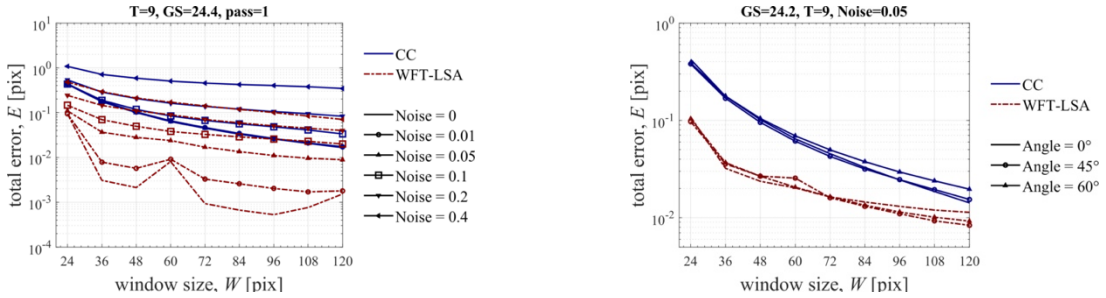

Figure 4: The effect of (a) increasing image noise and (b) grid angle on total error versus window size under uniform displacement.

Finally, it can be observed from Figure 4(b) that both methods are insensitive to the alignment of the grid with the camera field of view. More work needs to be performed to test the sensitivity of the WFT-LSA to slight deviation of the true grid angle and spacing as compared to the values used in processing the recorded images. Both of these parameters will play a role in determining the performance of the algorithm in non-uniform flow fields with significant shear and rotation. As will be seen in the next section, such effects may cause the performance of the method to drop below that of simple cross-correlation.

3.2. Sinusoidal flow and MTF comparisons

Although the WFT-LSA method showed improved performance for measuring the displacement of gridded patterns under uniform flow conditions, most flows of interest in fluid mechanics feature shear and rotation. To gain some insight into the method's behavior in these conditions, we calculated the MTF for sinusoidal displacement fields. As seen in Figure 5(a), both the standard PIV-style cross correlation algorithm and the WFT-LSA analysis attenuated the amplitude of the measured displacement field with nearly no change in shape, except near the image borders where the interrogation regions overlapped the edges. For nearly every combination of grid structure and spatial window size, the CC algorithm gave superior results. This attenuation decreased with increasing number of iterations using an image deformation algorithm between displacement estimates, but the relative separation between the two methods remained (Figure 5(b)). However, the displacement estimates are not fully converged, and the results indicate that the WFT-LSA may still approach similar MTF values as the CC method with a greater number of passes.

It was noted that normalizing the processing window size, W, and the grid spacing, GS, by the wavelength of the displacement fluctuations consistently collapsed the calculated MTF curves. To aid in visualizing the results over the large parameter space of different window sizes, grid spacings, and wavelengths, these results were collapsed into contour plots of MTF over normalized wavelengths.

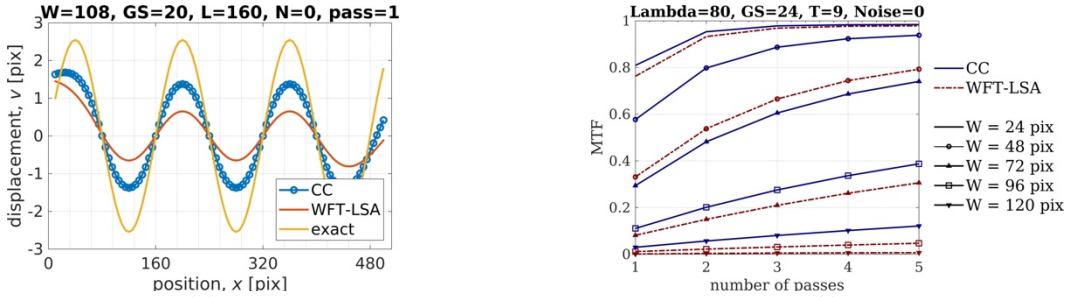

(a) (b)

Figure 5: (a) Example of amplitude modulation for a sinusoidal displacement field. (b) Increasing MTF with convergence of iterative processing.

In Figure 6(a), the MTF are plotted versus normalized frequencies ω_W and ω_{gs}. Plotted this way, the results are useful for determining the response of the velocity estimator to a fixed displacement wavelength, λ, using various window sizes and grid spacings. Here the space where $W < GS$ is mostly unsampled; it is anticipated that both methods would likely break down in this case as seen in Figure 3(a). Conversely, the normalized wavelength plots in Figure 6(b) are most useful for determining the range of resolvable wavelengths with a fixed value for W and GS.

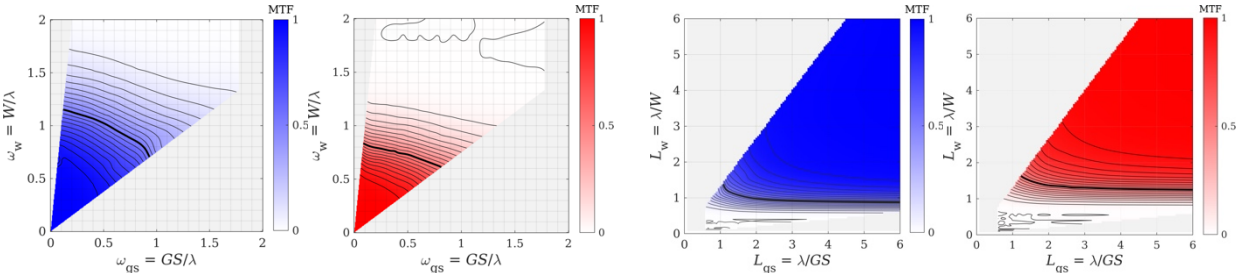

(a) normalized frequencies (b) normalized wavelengths

Figure 6: Plots of MTF after 5 passes for variations in window size, grid spacing, and flow wavelength. The heavy black lines indicate an MTF=0.5, and the light contours are spaced every 0.05 units.

In both sets of plots it can be seen that the region where the MTF > 0.5 is larger for the cross correlation processing than for WFT-LSA. For the CC method, to maintain high values of MTF the spatial window should be no larger than the smallest wavelength sampled, and ideally less than half that size. Similarly, the grid spacing should be on the same order as the flow wavelength, and ideally smaller. Similar trends are seen for the WFT-LSA method, though the cutoff for MTF = 0.5 is larger at ~0.75 W/λ. These results indicate that although WFT-LSA was better for uniform flow, under larger levels of spatial gradients this advantage breaks down. However, iterating the method through additional passes may still converge the resulting vector field much closer to the exact displacements; 5 passes was not sufficient for convergence.

4. Experimental validation and application to high speed flows.

The target for this study is to choose appropriate grid and processing parameters for MTV use in high speed gas flows (> 100 m/s). This is especially true since the grid geometry must be chosen ahead of time, and is difficult to adjust. To validate the results of the synthetic image testing described above, we have constructed a square channel flow loop instrumented for simultaneous PIV and MTV (Figure 7).

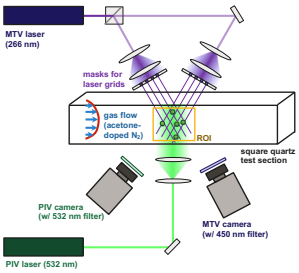

(a) schematic of simultaneous PIV/MTV experiment

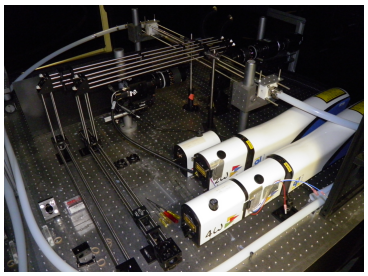

(b) image of experimental setup

Figure 7: A gas flow loop is being used to test the accuracy of MTV under realistic conditions

Both measurement systems are using Imperx 29 Mpix dual-frame CCD cameras supplied by TSI, binned using 8x8 superpixels. For the PIV acquisition, the flow is seeded using DEHS droplets using a Laskin nozzle. For use with MTV, the flow loop seeded using a chilled bubbler with acetone vapor near saturation concentrations, and is purged and driven with bottled nitrogen. For MTV acquisition, the camera is supplemented by a single-stage image intensifier manufactured by Photek using a P20 phosphor on the camera side for increased total efficiency. The flow rate in the loop is controlled by means of an Alicat flow controller at up to 150 SLPM of nitrogen prior to picking up the acetone and DEHS seeding. Gas composition during the experiment is monitored using a SRS QM300 residual gas analyzer. The test section is an extruded quartz channel with a square 25.4 mm cross section to allow maximum transmission of UV excitation and emission wavelengths. Illumination is provided by two Quantel Brilliant B lasers which are locked to 10 Hz operation. The first is frequency quadrupled to supply both the 532 nm and 266 nm harmonics which are split using a dichroic for both PIV and MTV use. The second laser is frequency doubled for the 532 harmonic for the second frame of PIV acquisition. Initial results (see Figure 8) have shown good image quality at the delays near 1 μs that will be required for use in the particle acceleration experiments in our shock tube facility, where small fields of view and post-shock speeds on the order of 100 m/s are expected. Work is ongoing to optimize the imaging for the slower flows achievable in the channel flow experiment.

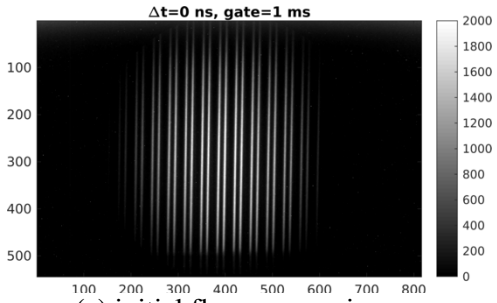

(a) initial fluorescence image

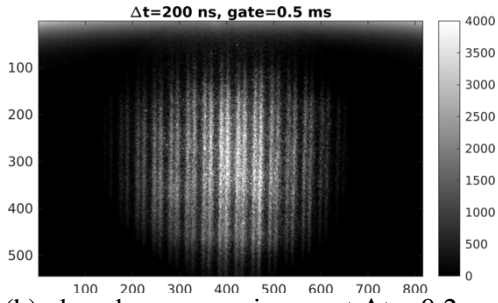

(b) phosphorescence image at $\Delta t = 0.2$ μs

Figure 8: Example MTV images

5. Discussion and Conclusion

Based on our initial synthetic image testing, the WFT-LSA method is a promising approach for measuring the displacement field in images of gridded patterns such as are typical in MTV. Performance is comparable to a standard cross correlation PIV implementation, with total error levels lower for flows with nearly uniform velocity, but increased attenuation of fluctuations as measured by the MTF of the method. However, the WFT-LSA method appears to be more resistant to higher noise levels in the raw images, and more tolerant of very wide illuminated line thicknesses. This is as compared to cross correlation, which performs the best with line thickness near 2-3 pixels, similar to the optimum particle size for PIV. Additionally, another factor that needs to be explored is whether WFT-LSA is more resilient to changes in intensity and increases in the grid thickness between the first and second image of a pair. Such effects are

common in gas-phase MTV due to diffusion (turbulent and molecular) and the rapid decay of the phosphorescence signal with time. Typically, when using acetone or a similar molecule as the tracer the first image in each pair will be a sharp and bright fluorescence image, while the second will be degraded.

One important fact to note about the WFT-LSA method is that it is considerably faster than a standard PIV implementation due to its focus on only a single characteristic wavelength in the Fourier transform step. For example, a single iteration (no image deformation) of the current MATLAB implementation of the cross correlation method returned 41×82 = 3,362 vectors in 10.1 seconds, while the WFT-LSA algorithm returned a vector on every pixel of a 512×512 image (262,144 vectors) in only 6.9 seconds. This has important implications for use with iterative algorithms, as the dense predictor for image interpolation can be provided without any additional velocity interpolation being required, and the method can be converged for many more iterations than for traditional correlation in the same amount of time. This factor needs to be further explored to see if parity with traditional cross correlation can be recovered.

6. References

Astarita T (2006) Analysis of interpolation schemes for image deformation methods in PIV: effect of noise on the accuracy and spatial resolution. Experiments in Fluids 40:977-987

Bordoloi AD, Martinez AA, Prestridge K (2017) Relaxation drag history of shock accelerated microparticles. Journal of Fluid Mechanics 823

Eckstein A, Vlachos PP (2009) Assessment of advanced windowing techniques for digital particle image velocimetry (DPIV). Measurement Science and Technology 20:075402

Gendrich CP, Koochesfahani MM (1996) A spatial correlation technique for estimating velocity fields using molecular tagging velocimetry (MTV). Experiments in Fluids 22:67-77

Grédiac M, Sur F, Blaysat B (2016) The Grid Method for In-plane Displacement and Strain Measurement: A Review and Analysis. Strain 52:205-243

Herráez MA, Burton DR, Lalor MJ, Gdeisat MA (2002) Fast two-dimensional phase-unwrapping algorithm based on sorting by reliability following a noncontinuous path. Applied Optics 41:7437-7444

Hiller B, Booman RA, Hassa C, Hanson RK (1984) Velocity visualization in gas flows using laser-induced phosphorescence of biacetyl. Review of Scientific Instruments 55:1964-1967

Kasim MF (2019) Fast 2D phase unwrapping implementation in MATLAB. https://github.com/mfkasim91/unwrap_phase/

Koochesfahani MM, Nocera DG (2007) Molecular tagging velocimetry. In: Tropea C, Yarin AL and Foss JF (eds) Handbook of experimental fluid dynamics. Springer, Berlin, Heidelberg, pp. 362–382

Miles RB, Lempert WR (1997) Quantitative Flow Visualization in Unseeded Flows. Annual Review of Fluid Mechanics 29:285-326

Ragni D, Schrijer F, van Oudheusden BW, Scarano F (2011) Particle tracer response across shocks measured by PIV. Experiments in Fluids 50:53-64

Sanchez-Gonzalez R, McManamen B, Bowersox RDW, North SW (2015) A method to analyze molecular tagging velocimetry data using the Hough transform. Review of Scientific Instruments 86:105106

Stier B, Koochesfahani MM (1999) Molecular Tagging Velocimetry (MTV) measurements in gas phase flows. Experiments in Fluids 26:297-304

Surrel Y (1994) Moire and grid methods: a signal-processing approach International Conference on Interferometry '94. Society of Photo-Optical Instrumentation Engineers, pp. 118-127